Welding in the World (2019) 63:1205–1220
https://doi.org/10.1007/s40194-019-00743-y

RESEARCH PAPER

Numerical and experimental analysis on the influence of surface layer on the resistance spot welding process for the aluminum alloys 5182 and 6016

Stefan Heilmann[1] · David Köberlin[1] · Marcel Merx[2] · Jens Müller[2] · Jörg Zschetzsche[1] · Steffen Ihlenfeldt[2] · Uwe Füssel[1]

Received: 27 November 2018 / Accepted: 2 May 2019 / Published online: 22 May 2019

Abstract
Resistance spot welding is used as a high-productivity joining process for the increasing use of lightweight materials in industrial applications. The main challenge for the welding of aluminum alloys is the wear of the electrodes. Due to the natural oxide layers on the metal surface, high contact resistances exist between the sheet metal and the electrode. This results in increased heat generation at this interface, which leads to increased alloyage on the electrode. Breaking the insulating natural oxide layers can be achieved by a friction-free or friction-assisted motion overlay and leads to a reduced electrode wear. The complex physical correlations involved are currently being investigated in a basic research project at TU Dresden. In addition to welding tests on a test rig, simulation-based analyses are also carried out. These allow a physic-based modeling of the effects and can be used later on for an extrapolation of any resistance welding process with motion overlay. In this paper, first experimental and analytical considerations for the mechanical destruction of the oxide layer of aluminum are discussed. Subsequently, the developed extended simulation model is presented and compared according to the quality of simulation of the welding process with motion overlay. The simulation method used is a multiphysics FEM simulation with ANSYS.

Keywords Aluminum alloys · Resistance spot welding · Resistance welding electrodes · Contact resistance · Fem simulation

1 Motivation

The resistance spot welding process is an established process in thin sheet processing. It is mainly used in car body construction, predominantly to connect steel sheets together. The cohesive connection is formed by a current I, which is passed through two electrodes and the sheets to be joined. As a result of the law of Joule, which is described in Eq. 1, a quantity of heat Q is generated. The heat generated depends not only on the current I and the resistance of the system R_{tot} but also on the welding time t_w.

$$Q = \int_{t=t_0}^{t=t_w} \mathrm{I}^2(t) \cdot R_{\mathrm{tot}}(t)\, dt \tag{1}$$

The resulting temperature during the joining process depends on the heat flow $\dot{Q}$, i.e., the amount of heat transferred over a period of time. The most important influencing factors for the location- and time-dependent temperature are shown in Fig. 1.

It can be seen that the temperature depending on time and thus, the formation of a weld nugget is a very complex process. The influence of the material parameters and the change of the contact surface during the welding process can only be accurately represented by means of simulation.

Referring to Fig. 1 and Eq. 1, the total resistance R_{tot} can be identified as one of the most important parameters changing during the process. The total resistance consists of the material resistances R_1, R_3, R_5, and R_7 and the contact resistances R_2, R_4, and R_6. At the beginning of the welding process, the

Recommended for publication by Commission III - Resistance Welding, Solid State Welding, and Allied Joining Process

✉ Stefan Heilmann
stefan.heilmann@tu-dresden.de

Marcel Merx
merx@iwm.mw.tu-dresden.de

[1] Institute of Manufacturing Technology, Chair of Joining Technology and Assembly, Technische Universität Dresden, Dresden, Germany

[2] Institute of Machine tools and Control Engineering, Technische Universität Dresden, Dresden, Germany

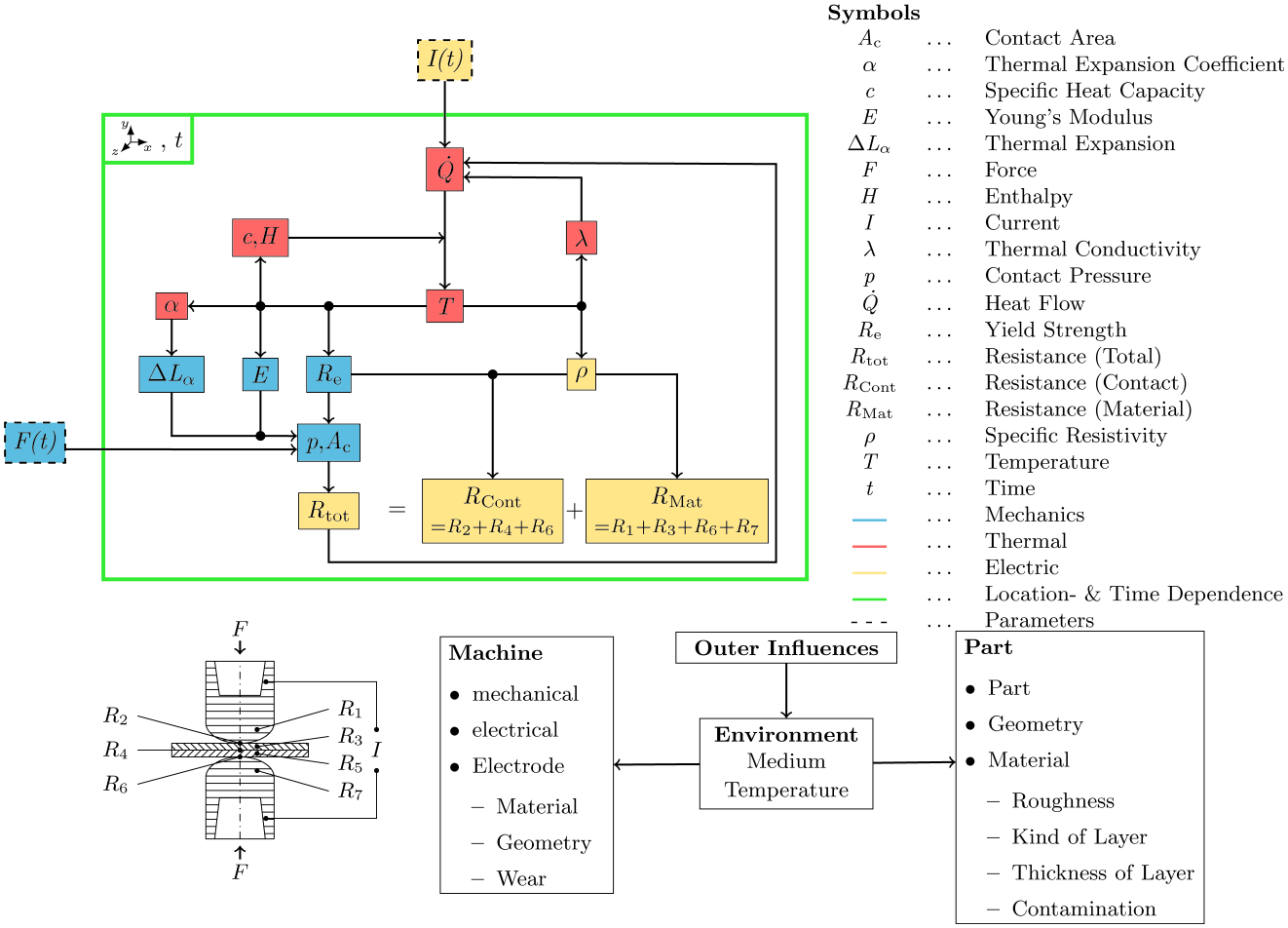

Fig. 1 Schematic overview of the influences on the resistance spot welding process

contact resistances are at their highest and decrease significantly with increasing time due to improved contact conditions between electrodes and sheets as well as in the contact between both sheets.

The influence of contact resistance is the greatest challenge for the reliable and cost-effective joining of aluminum materials by resistance spot welding. This depends directly on the insulating natural oxide layer on the aluminum surface. The oxide layer is irregularly pronounced in its composition and thickness over the entire surface and therefore always causes different initial conditions during welding. In addition, the increased contact resistance leads to a locally limited heating between the electrode and the sheet metal. Temperatures up to the softening range of the commonly used CuCr1Zr alloy are possible. In combination with the high affinity between copper and aluminum, this leads to increased electrode wear and consequently to constantly changing contact conditions. Due to changing initial conditions, with regard to contact resistance, no reproducible welding result with constant welding parameters is possible.

In order to be able to use resistance spot welding for joining aluminum materials cost-effectively, e.g., in car body construction, the resistance of the aluminum surface must be reproducibly reduced. The usual solutions concentrate on the chemical modification of the contact zone by chemical or physical processing [1–3]. Generally, it is problematic that the corresponding surface treatment cannot be carried out directly before the welding process. As a result, the oxide layer may form again in the time window between pre-treatment and the welding process. A promising alternative approach is the mechanical destruction of the oxide layer. In principle, frictionless or friction-free relative movements between the electrode and the sheet metal can be carried out either immediately before or during the current flow. Figure 2 shows three types for motion overlay. These are as follows: a rolling frictionless (a in Fig. 2: rotation in φ_Y), a combined relative movement (b in Fig. 2: rotation around in φ_Y and translation in X), and a sliding frictional movement (c in Fig. 2: translation in X) between electrode and sheet metal. A frictional motion overlay by rotating both electrodes around Z is already successfully used on an industrial scale in the "*RoboSpin*" process [4].

Another possibility for process-parallel mechanical destruction of the aluminum oxide layer is the patterning of electrodes. This can be done by mechanical [5, 6] or thermal [2] methods.

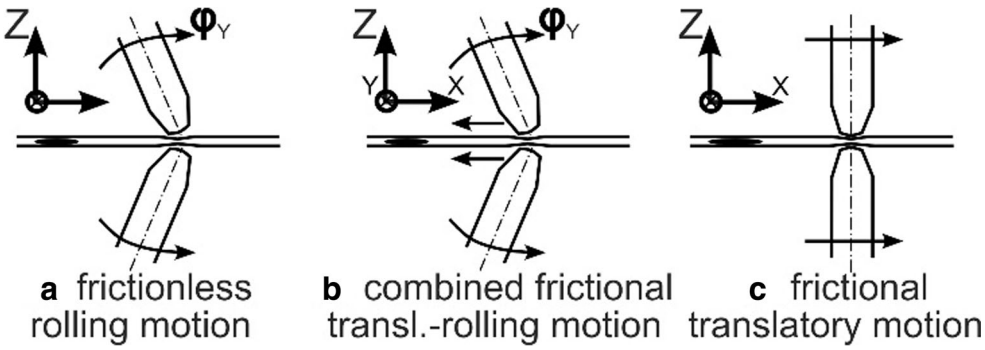

Fig. 2 Process variants of resistance spot welding with motion overlay [3]

However, the fundamental knowledge of the chemical and physical processes involved in the mechanical destruction of the oxide layer is still lacking.

2 Basic investigations on the behavior of the oxide layer

2.1 State of the art

For the description of the behavior of the oxide layer during resistance spot welding of aluminum alloys, only a few very specific findings are available so far. In previous work [7–9], predominantly empirical model approaches for contact modeling, in particular electrical contact resistance, have been developed and used. Up to now, the parameterization of the contact models has been done empirically on the basis of the evaluation and adjustment with welding tests. A well-founded investigation of the contact characteristics during resistance spot welding, in particular with respect to the relative movement of the contact partners, has so far only been carried out by Crinonen et al. and James et al. [10, 11]. A new study by Deng et al. [12] shows the influence of the destruction of the oxide layer by textured electrodes on the nugget formation.

2.2 Analogy experiments on the behavior of the oxide layer

In order to investigate the destruction of the oxide layer, experiments on a special test setup were done. The results obtained in these analogy experiments were finally validated by means of a FE analysis and can be transferred to the welding process on the basis of the surface pressures achieved.

For the execution of the analogy experiments for frictional motion overlay between electrode and sheet metal equivalent to C in Fig. 2, a scratch tester was modified (see Fig. 3). In the setup, the sheet metal is mounted on a cylindrical counter electrode and pulled underneath the upper electrode with a constant feed of 150 mm/min. A constant normal force F_Z is applied during the test. The normal force F_Z and the frictional force F_X are measured to calculate the friction coefficient μ. The determined friction coefficient can be used to estimate the wear condition of the electrode and is needed for the parameterization of the FE analysis. The destruction of the oxide layer during the movement is detected by the voltage drop over the contact at a constant current adjusted to 50 A. For the electrodes, the types F0–16 and F0–20 (spherical, according to DIN EN ISO 5821 [13]) were selected in order to be able to cover the relevant range of contact pressure, enabling a plastic deformation in the contact interface.

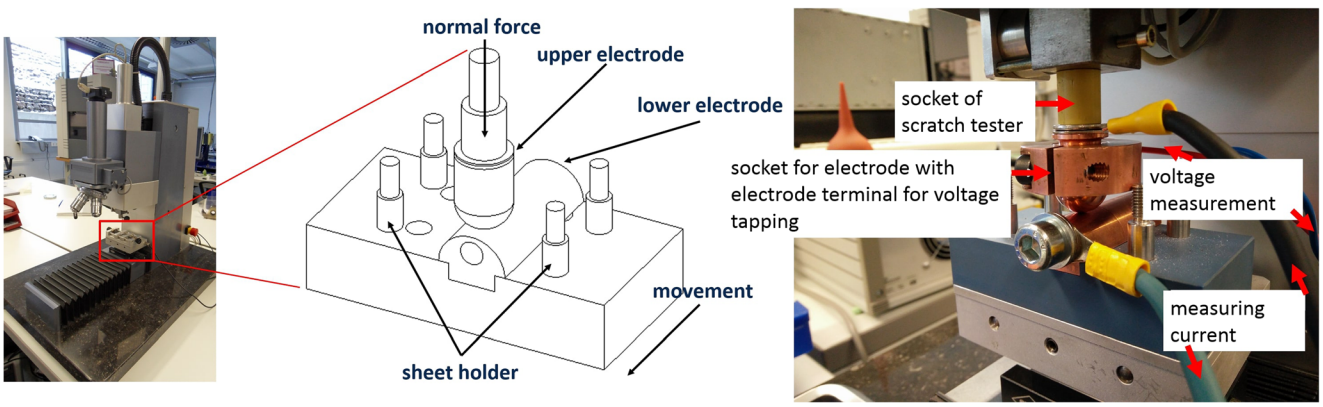

Fig. 3 Experimental setup for the investigation of the destruction of the oxide layer in case of frictional motion overlay

Two aluminum alloys, two electrode diameters, and four oxide layer thicknesses were investigated experimentally (see Table 1). Different oxide layer thicknesses were achieved by aging the sheets in a salt-spraying chamber. In order to enable the tests to be statistically verified, 6 tests were carried out for each configuration. This resulted in a total of 288 experiments.

In Fig. 4, for example, the progress of the normal force F_Z and the determined friction coefficient μ are plotted over the traverse path of the sheet metal. While the scratch tester keeps the contact force F_Z approximately constant, the coefficient of friction μ increases linearly over the traverse path. This effect is presumably due to the increasing immersion of the electrode during scribing or wear of the electrode. The mean coefficient of friction over the entire travel motion is used as a comparison value.

In Fig. 5, the total resistance in the contact electrode sheet electrode at a constant measuring current of 50 A is shown. When the sheet metal begins to move at approx. 1 s, a significant decrease in the total resistance is visible as a result of the destruction of the oxide layer of the aluminum. For the quantitative evaluation of this drop in resistance, the averaged values before and after the start of movement were used.

The whole of the measurements show a significant decrease in contact resistance correlating to the start of movement (compare Fig. 5). The value of this drop depends on the respective configuration of the material, the electrode cap diameter and the selected contact force, and the wear condition of the electrode. On average, over all experiments, the resistance drop amounts to approx. 50% of the initial value before motion.

In Fig. 6, the experimentally determined friction coefficient μ is shown for the two alloys EN-AW-5182 and EN-AW-6016. It becomes clear that the coefficient of friction increases with increasing aging time from zero to 10 days.

The comparison of the total resistance between electrode, sheet metal, and counter electrode before the start of each movement (see Fig. 7) confirms the expected correlation. With increasing aging time, i.e., greater oxide layer thickness, the contact resistance also increases. With regard to the influence of the electrode radius, two opposing effects occur. On the one hand, a smaller electrode radius (F0–16) results in higher contact pressure, which leads to a better leveling of the roughness peaks on the contact surface and thus to a lower contact resistance. On the other hand, a larger electrode radius (F0–20) also results in a larger total contact area, which also leads to a reduction of the contact resistance. In Fig. 7, the effect of the higher surface pressure seems to dominate, at least for the alloy EN-AW-5182, since the experiments with electrodes F0–16 show a lower resistance value compared with the electrodes F0–20. The overall higher resistance of the experiments with EN-AW-5182 can be explained by the higher specific resistance of this alloy.

In Fig. 8a, the resistance measurement over time is shown for two scratch tests. Jumps in the measured resistance can be detected during the movement phase. It has

Table 1 Parameter overview for the investigation of the destruction of the oxide layer in case of frictional motion overlay

Alloy	EN-AW-5182, EN-AW-6016
Normal force	60 N, 100 N, 30…100 N (rising)
Aging	0 days, 1 day, 3 days, 10 days
Electrode types	F0–16, F0–20

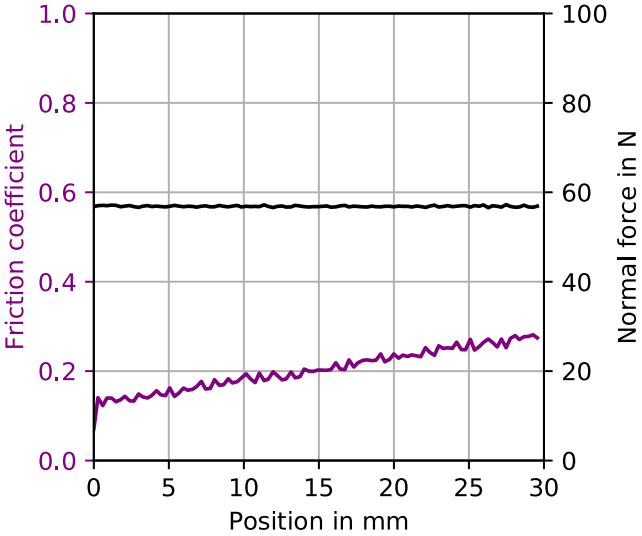

Fig. 4 Friction coefficient over traverse path for EN-AW-5182 sample

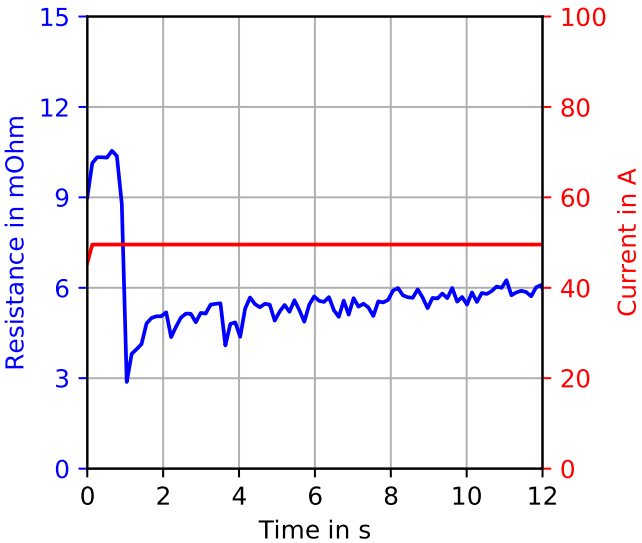

Fig. 5 Total resistance over time for EN-AW-5182 sample (motion starting at approx. 1 s)

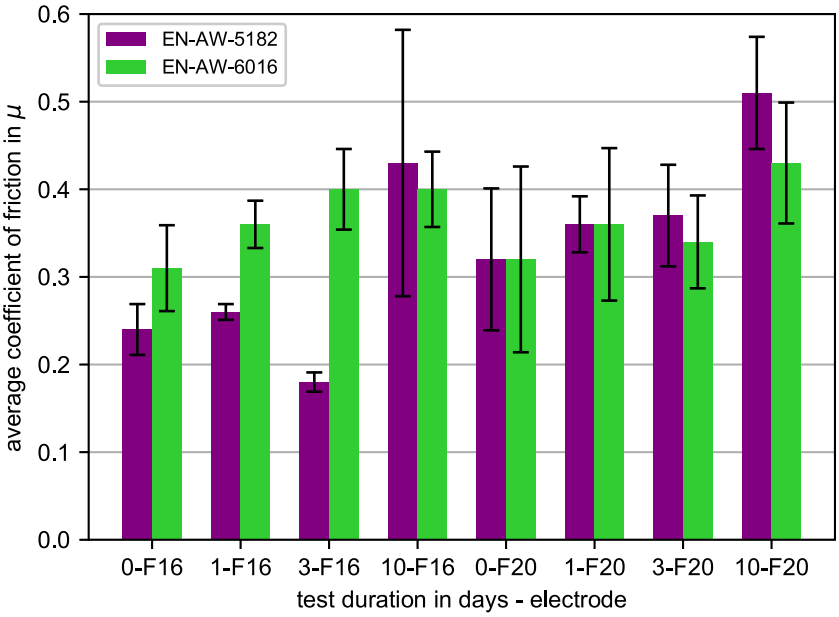

Fig. 6 Determined averaged friction coefficients μ as a function of aging time (0, 1, 3, or 10 days) for the two alloys EN-AW-5182 and EN-AW-6016 and electrode caps F0–16 (F16) and F0–20 (F20)

been assumed that these result from an aggregation of material in front of the electrode. In order to be able to characterize the mentioned effect of the material accumulation more precisely, confocal images were made for the respective samples. In addition, for the highlighted areas (red marking in Fig. 8b) a detailed confocal image was taken (see Fig. 8c). This image shows the trace of the electrode (blue coloration) and the accumulation of material within the trace (red coloration). The detailed confocal image confirms that the relative movement of the electrode leads to a plastic deformation of the sheet surface. This destroys and displaces the oxide layer of the aluminum and creates a direct metallic contact. If too much material is piled up in front of the electrode, it "jumps" over the material aggregation, which, as expected, results in a locally increased contact resistance.

2.3 Simulative analysis of the mechanical processes involved in the destruction of the oxide layer

In order to be able to better interpret the results of the analogy test, a quasi-static FE analysis was created in ANSYS Workbench (ANSYS® Academic Research Mechanical, Release 16.2.). In the model, the symmetry in the sheet metal plane and in the *X-Z* plane of the electrode is used to minimize the number of elements (see Fig. 9a). Plastic deformation of the EN-AW-6016 alloy (sheet) and the CuCr1Zr (electrode) is possible by considering the materials yield stresses and the

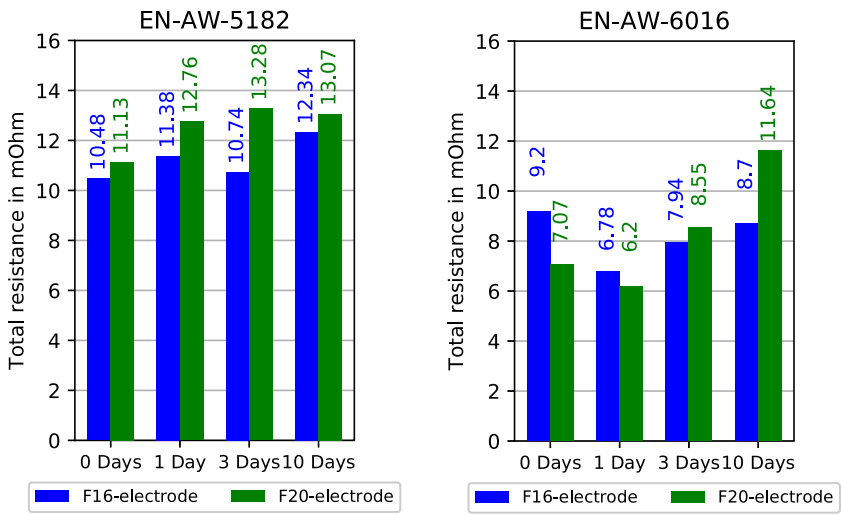

Fig. 7 Determined total resistance values (just before motion) as a function of aging time for the two alloys EN-AW-5182 und EN-AW-6016 and electrode caps F0–16 (F16) and F0–20 (F20)

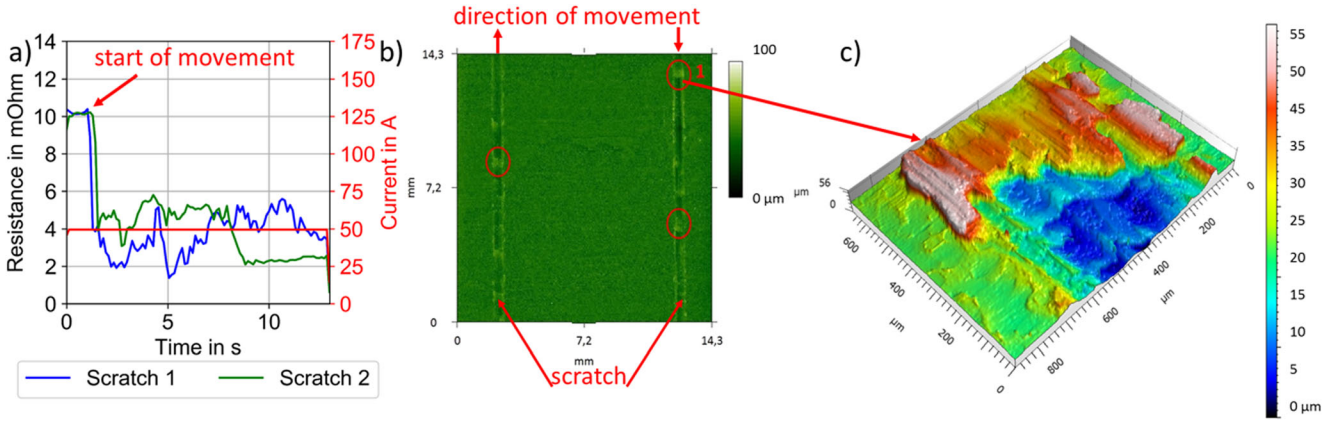

Fig. 8 Frictional motion overlay: **a** resistance over time for two motions, **b** confocal image of scratches generated by moving electrode, **c** detail of the confocal image shown in **b**

tangential moduli. The coefficient of friction between electrode and sheet metal was calculated as an average value from Fig. 6 and set to $\mu = 0.35$. The application of a single axial force $F_Z = 100$ N (see Fig. 9b) was defined as the reference case. In addition, a translational motion overlay in the *X*-direction, applied in small steps up to a maximum value of approx. 0.065 mm (see Fig. 9c), and a rolling motion overlay as rotation around the *Y*-axis, applied in small steps up to a maximum value of approx. 0.050° (see Fig. 9d), each with a contact force $F_Z = 100$ N, were implemented. The simulation results in Fig. 9 show that even at low contact forces, sufficiently high stresses are generated. These lead to plastic deformation of the base material and thus reliably destroy the oxide layer when a relative motion is applied. For example, the surface pressure is already approx. 950 N/mm^2 (see Fig. 9b) for a normal force of 100 N in the *Z*-direction. The corresponding friction stress (not shown in the figure) is 32.7 N/mm^2 at maximum.

In the case of the frictional translational motion overlay (see Fig. 9c), the maximum surface pressure occurs in the area in which the sheet metal flows under the electrode against the direction of motion. The maximum frictional stress results directly below the electrode tip. The friction stress occurring is approx. 176 N/mm^2 and is thus more than five times greater than with pure force application in the *Z*-direction. The resulting scribing trace (plastic area) has a width of about 0.4 mm, which corresponds to the measurement results of confocal microscopy in Fig. 8c. The higher maximum surface pressure of approx. 1176 N/mm^2 (compared with Fig. 9b) can be explained well by the superposition of contact and feed force at the electrode radius.

Compared with the original hypothesis of a theoretically frictionless, rolling superposition of motion (compare A in Fig. 2), it can be seen that significant frictional stresses also occur within the rolling relative motion in Fig. 9d. Only a narrow strip with low friction stress (i.e., almost ideal rolling) is formed in the middle of the electrode (see Fig. 9d). The directly adjacent areas experience a higher frictional stress, probably due to the lower effective electrode rolling radius. This stress is at approx. 163 N/mm^2 and thus in the same order of magnitude as with the frictional translation in Fig. 9c. This should lead to a comparable effect in the destruction of the oxide layer. The resulting maximum surface pressure of approx. 1216 N/mm^2 is also in a similar order of magnitude.

Since a combined frictional-rolling relative motion overlay (compare B in Fig. 2) can be represented as a combination of the abovementioned variants, comparable effects are expected.

After the effect of the destruction of the oxide layer by motion overlay could be proven within the analogy experiments and the corresponding simulations, the experimental equipment developed for the realization of welding tests is described in the following section.

3 Test rig for resistance spot welding with motion overlay

3.1 Design and functionalities of the test rig

For the conventional resistance spot welding process, a kinematic system is required which positions the electrodes at the joint, applying the required contact pressure via the electrode force. In addition, a low-resistance current transmission to the electrodes as well as cooling of the electrodes must be ensured. In the case of the resistance spot welding processes with motion overlay according to Fig. 2, two additional axes of motion are added to the infeed-axis *Z*. The first additional axis is the translation of the sheet in the *X*-direction, carried out with a maximum feed force of $F_X = 6$ kN at the developed test rig (see Fig. 10a) in accordance with the friction

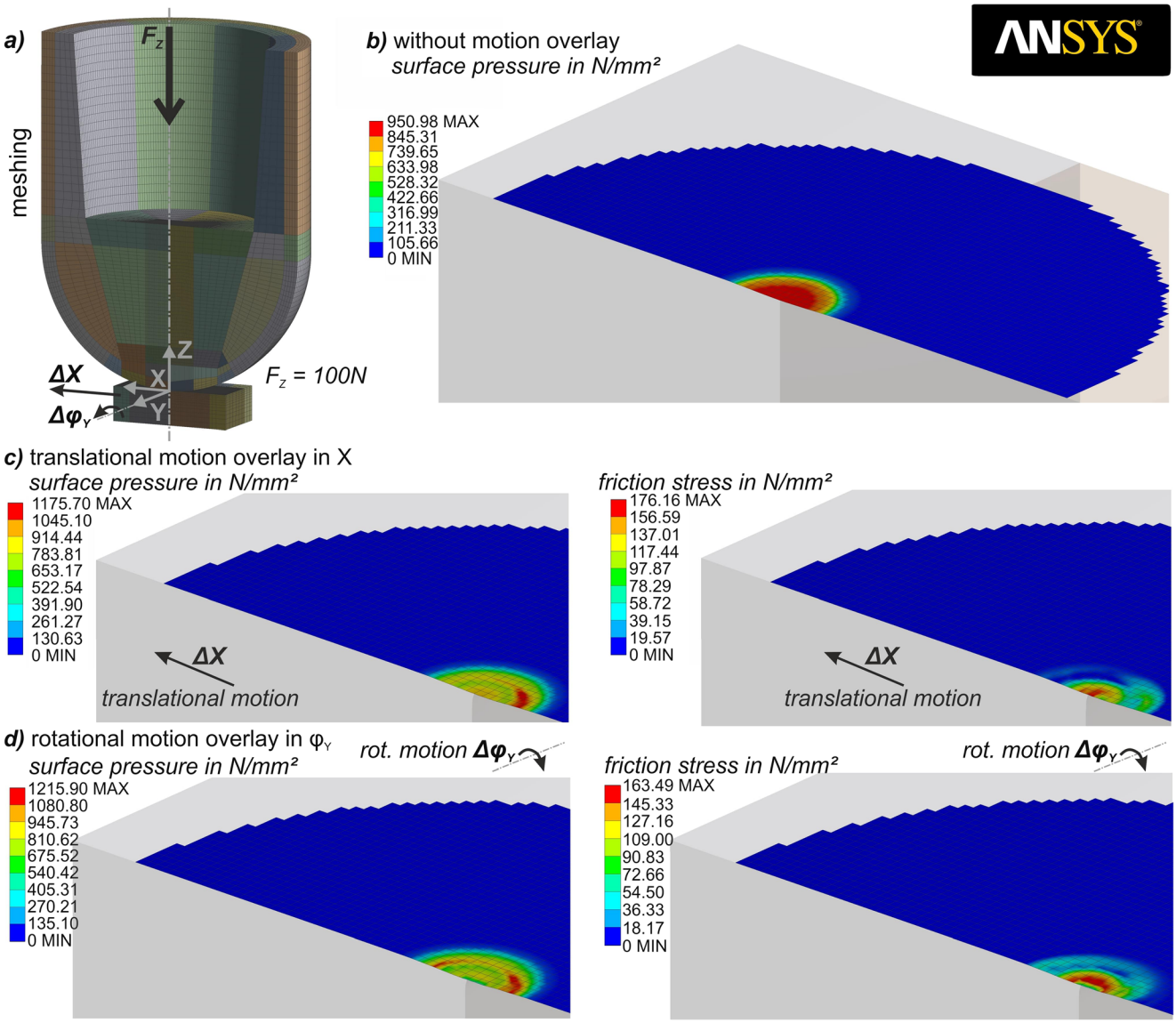

Fig. 9 Modeling and simulative results for frictional motion overlay (EN-AW-6016 alloy, F16 electrode cap), **a** model and mesh, **b** surface pressure without motion overlay, **c** surface pressure and frictional stress with translational motion overlay of max. 0.065 mm (compare C in Fig. 2), and **d** surface pressure and frictional stress with rotational motion overlay of max. 0.050° (compare A in Fig. 2)

coefficients derived from the analogy experiments in Section 2.2. The second additional axis is the rotation of the electrode heads (see Fig. 10b), which, when designed for a maximum swivel angle of $\varphi_Y = \pm 45°$, results in a maximum torque of 1100 Nm. In the *Z*-direction, the infeed can apply a maximum force of $F_Z = 15$ kN on the electrodes.

The kinematics of the test rig are based on a solid welded base frame made of hollow steel profiles (see Fig. 10a). A solid base plate holds the profile rail guides of the *Z*-slides and those of the sheet feed's holding frame (motion in *X*-direction), respectively. The sheet feed working in the *X*-direction is driven by a linear unit with ball screw drive. A total of 16 test sheets, each of 50 × 50 mm in size, can be clamped in the holding frame of the sheet feed unit. In order to achieve high precision, all guides and the electromechanical drives of the test rig are designed with zero backlash. The two electrode heads (see Fig. 10b) have an integrated cooling water circuit and are designed to be equipped with standardized electrode caps with a nominal diameter of 16 or 20 mm according to DIN EN ISO 5821 [13]. A pneumatically driven electrode milling device is used for the dressing of the electrodes. The current source is a medium frequency inverter (f_{PWM} = 1000 Hz), which can provide currents of up to 50 kA via two parallel connected welding transformers. Further information on the construction and the simulation-based design of the test rig can be found in [14].

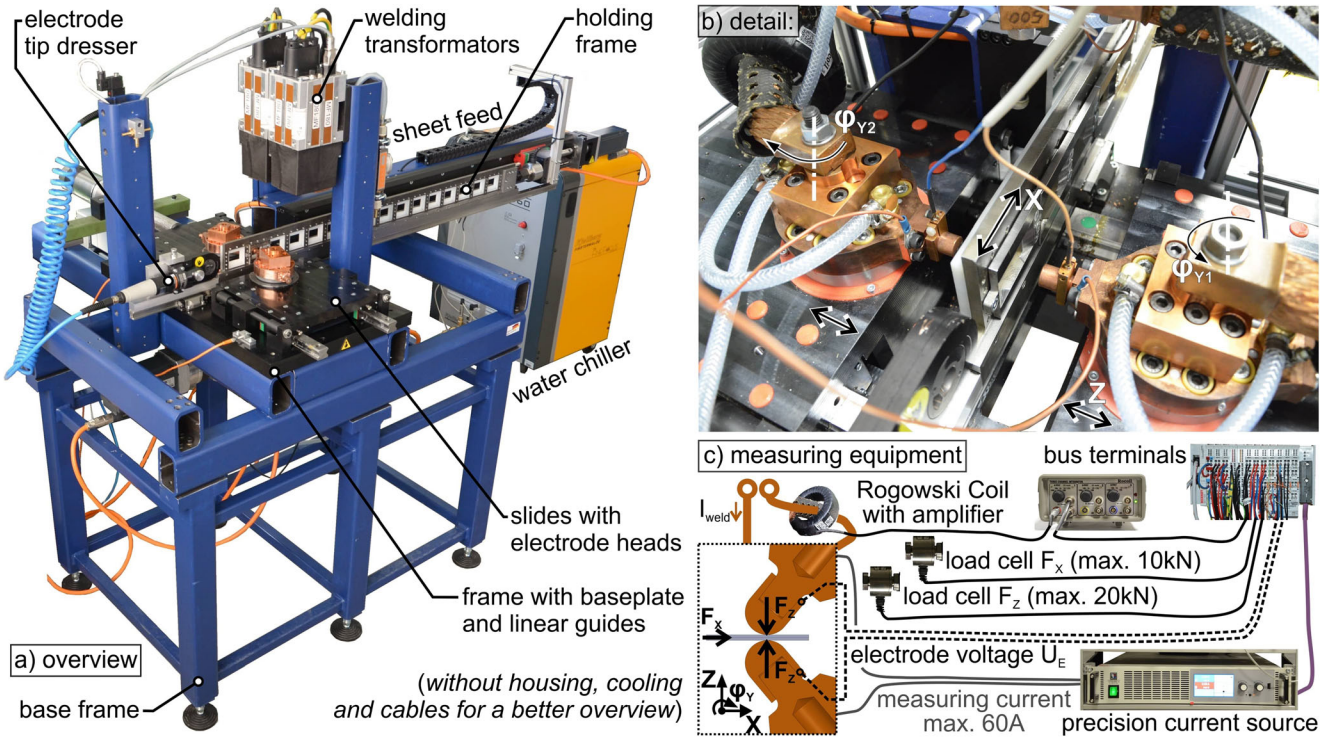

Fig. 10 Test rig for resistance spot welding with motion overlay: **a** overview, **b** detail of the electrode arrangement, and **c** integrated measuring systems

In Fig. 10c, the measurement chain for data acquisition integrated in the test rig is shown. The contact force of the electrodes F_Z and the feed force of the sheet feed unit F_X are measured via load cells with integrated bridge amplifiers. Thus, the friction coefficient between electrodes and sheet metal can be derived. The welding current is measured by means of a Rogowski coil in the power supply line to the electrodes. The measurement of the voltage drop over the electrode sheet electrode contact (electrode voltage U_E) is carried out by means of copper clamps mounted on the electrode caps (see Fig. 10b). The bus terminal used for voltage measurement enables a resolution of approx. 1.2 μV. The copper clamps also contain thermocouples for measuring the temperature of the electrode caps. Further temperature sensors monitor the temperature in the cooling circuit. To determine the contact resistance prior to the actual welding process, a precision current source controlled via ProfiBus imprints a maximum measuring current of 60 A into the electrode sheet electrode combination. The total resistance can be determined by measuring the voltage U_E at the electrodes. For an integrated system resistance measurement, a gold-plated copper sheet, clamped in one of the 16 holding frames, is used.

As the listed measuring systems are all evaluated via bus terminals in the control cabinet, the measurement data are immediately available in the control system of the test rig. They are thus automatically synchronized with the motions of all axes and can be displayed and stored on the control PC with a sample time of 250 μs (sample rate of 4 kHz). The force signals F_X and F_Z such as the current I, measured by the Rogowski coil, are sampled with 100 kHz and averaged to fit the 4-kHz data acquisition rate of the control system.

3.2 Experimental procedure

For the first experimental proof of the positive effect of the destruction of the oxide layer on the characteristics of the welding process and the electrode wear, 3 experiments comprising a series of four welds each were carried out. One experiment contains the classic resistance spot welding process without motion overlay; 2 experiments were carried out applying a frictional motion overlay according to C in Fig. 2. For the experiments, 2-mm thick sheets of EN-AW-6016 in the T4 state (no additional aging in the salt-spraying chamber) and electrode caps of the type A0–16 according to DIN EN ISO 5821 [13] (40-mm radius at the tip) of CuCr1Zr are used. The welding current was set to 46 kA at a welding time of 60 ms. The current profile used was determined on the basis of empirical values. The values are selected in such a way that the criterion for the welding lens diameter of at least $5\cdot\sqrt{t}$ (t = sheet metal thickness) is achieved.

Since, according to the confocal images shown in Fig. 8, there may be an accumulation of material in front of the electrode, a short distance of 1 mm was chosen for translational motion overlay. In order to realize multiple scribing in the same path, a sinusoidal movement for the sheet feed was created. The movement takes place before the actual welding

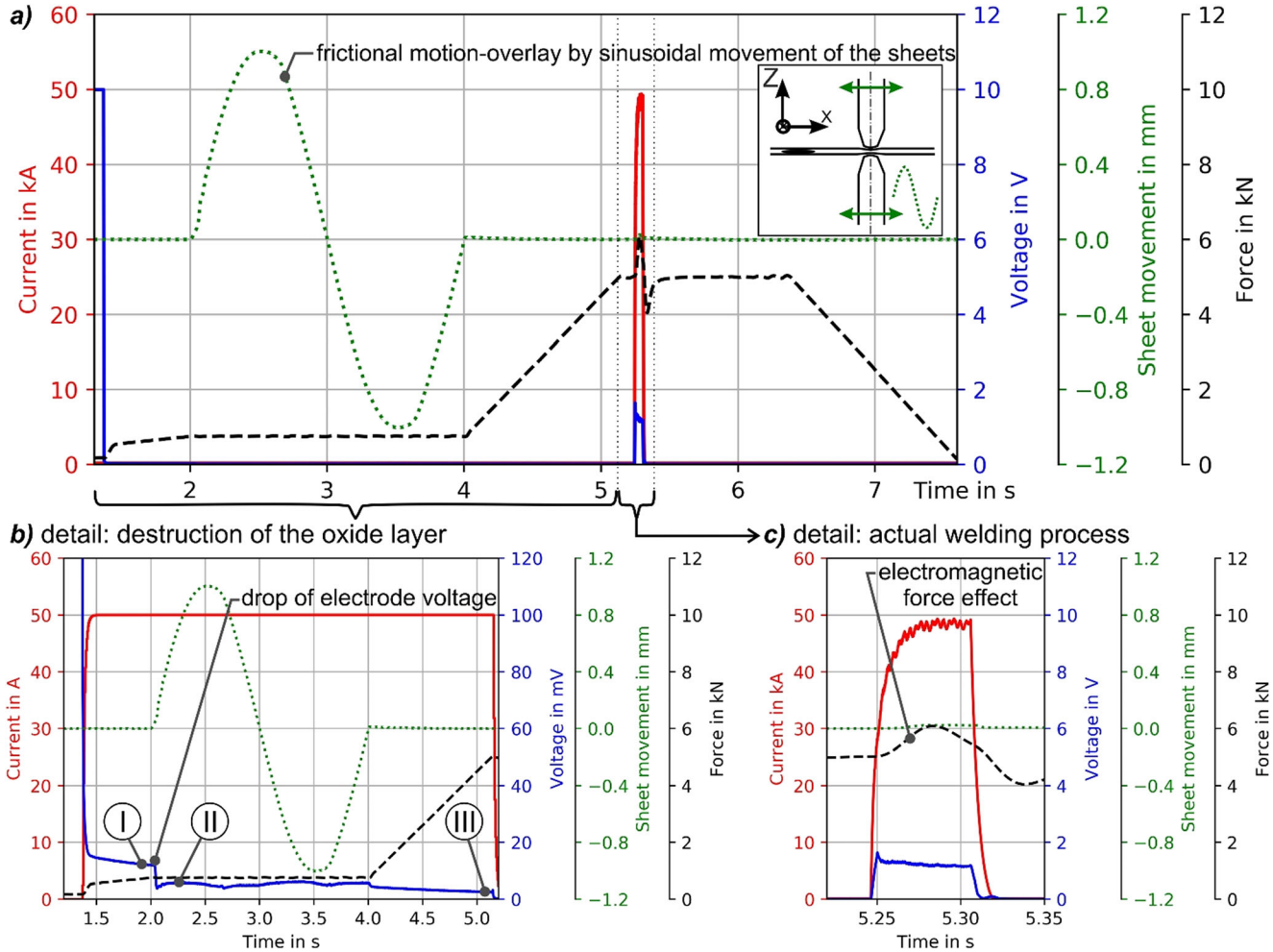

Fig. 11 Characteristic process parameters recorded at the test bed: **a** overview, **b** detail of the destruction of the oxide layer, **c** detail of the actual welding process

process with a pressing force of $F_Z = 750$ N. The electrode is no longer lifted from the sheet metal after "scribing" to avoid regeneration of the oxide layer.

3.3 Evaluation of the experiments

In Fig. 11a, the characteristic process parameters recorded at the test bed are shown as an example for frictional motion overlay before the actual welding. Based on the graph of the contact force F_Z and the electrode voltage U_E, the moment of contact between sheet metal and electrodes at approx. 1.25 s can be assigned. At this moment, the measuring current source reduces the voltage, which is limited to a maximum of 10 V, until the set measuring current of 50 A is reached (see detail in Fig. 11b). When the sheet metal feed starts moving, the celetroce voltage (and thereofe alse the contact resistance) drops, which is due to the desired effect of the destruction of the oxide layer. After the sheet feed has been completed, the electrode force F_Z is increased to 5 kN. Shortly before the welding current is switched on, the measuring current source is switched off. When the welding current is switched on, the welding voltage is measured via the copper clamps on the electrodes (see detail in Fig. 11c).

During the current passage, a significant fluctuation is visible in the force signal, which is due to electromagnetic forces acting between the two slides. On the other hand, when welding aluminum, there is an increased thermal expansion of the workpieces, which causes the sheets to be pressed onto the electrodes and thus leads to an increase in force.

For the purpose of better comparison of the experiments, characteristic values can be derived from the curves of the measured variables illustrated in Fig. 11. From the electrode voltage U_E and the known measuring current, the total resistance values are obtained before the motion (I in Fig. 11b), during the motion (II in Fig. 11b) and shortly before the welding current flow (I in Fig. 11b). The measured feed force F_X (not shown in the figure) and the known contact force F_Z can be used to determine the coefficient of friction during

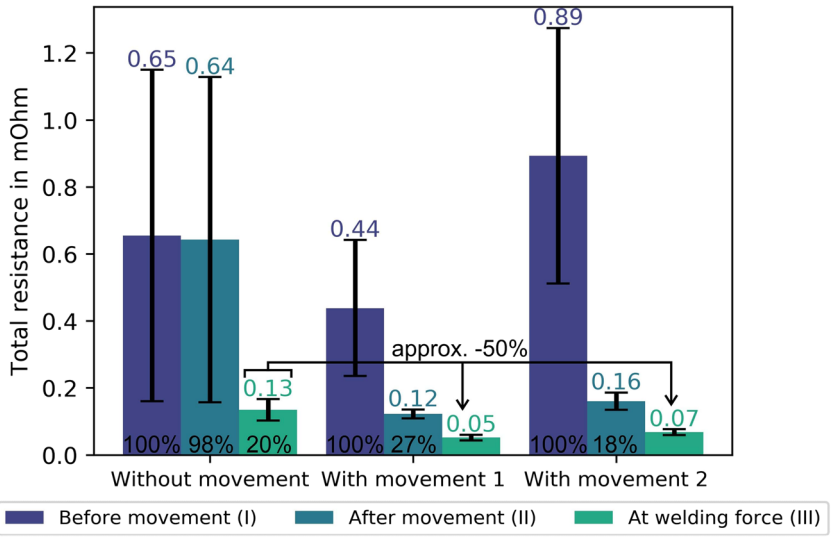

Fig. 12 Comparison of resistances with and without movement at three different points in time I to III (compare I with III in Fig. 11b)

frictional motion overlay. Finally, cross-sections can be used to compare the welding lens produced in the experiment with a welding lens predicted by means of a simulation.

In analogy to the process shown in Fig. 11, the reference process was carried out without motion overlay but with the identical specifications for electrode force F_Z (first at 750 N and then at full 5 kN), welding current and welding time. New electrode caps were used for each of the 3 experiments.

As demonstrated by the preliminary tests at the scratch tester, the total resistance is approx. Halved when the oxide layer is destroyed by relative movement (compare Fig. 5). This insight was confirmed by the described experiments at the test bed. In Fig. 12 the determined total resistances of the experiments with and without motion overlay at three different points in time (compare I with III in Fig. 11b) are shown. For the experiment without movement, the values "before movement" and "after movement" in Fig. 12 correspond to the state at different measuring times according to Fig. 11b. All values shown in Fig. 12 were averaged from 4 samples. Additionally the root mean square deviation was calculated. The experiments with movement were carried out twice ("with movement 1" and "with movement 2" in Fig. 12). The electrodes were treated with abrasive paper to remove the copper oxide layer and cleaned with ethanol directly before each experiment. The electrodes were changed between the experiments (3 pairs of electrodes).

Due to the locally varying thickness of the oxide layer, the resistances before the movement (I in Fig. 12) have a large scattering range. The comparison of the three measurement series also reveals differences in the absolute resistance range. This can also be attributed to different initial states of the electrodes. Through motion overlay the oxide layer is destroyed, what is evidenced by the drop of the total resistance from I to II (see "with movement 1" and "with movement 2," in Fig. 12). In contrast to the preliminary tests at the scratch tester, the resistance decreases to approx. 27% resp. 18% of the initial value. This difference to the analogy experiments can be explained by the changed electrode geometry, the higher normal force, and the locally different oxide layer. The destruction of the oxide layer results in a more uniform contact resistance, which is evident from the decreasing standard deviation. This results in reproducible total resistances, which leads to a more reproducible welding process.

The resistance just before the welding process is indicated by the third bar ("at welding force," III) in Fig. 12. As the experiments without movement show a reduction of the resistance to about 20% of the initial value before movement (I), the increase in normal force may also cause the oxide layer to break up. However, since the remains of the oxide layer cannot be removed underneath the electrode, there is a higher resistance compared with the experiments with movement when full pressing force of 5 kN is applied. The comparison

Table 2 Thermal and electrical material properties for EN-AW-6016 (sheet material)

Temperature (°C)	20	200	300	500	570
Specific resistivity (Ωm)	3.4E−08	5.19E−08	6.33E−08	9.1E−08	1.079E−07
Thermal conductivity (W/m K)	158	163	163	154	183
Heat capacity (J/g K)	0.886	0.936	0.947	1.018	1.042
Density (g/cm^3)	2.696	2.662	2.64	2.594	2.576
Thermal expansion coefficient (ppm/K)	–	23.46	24.96	26.91	27.9

Table 3 Mechanical material properties for EN-AW-6016 (sheet material)

Temperature (°C)	20	100	200	400	500
Young's Modulus (GPa)	72.63	69.21	64.8	56.57	53.64
Shear modulus (GPa)	26.82	25.79	24.22	21.27	20.27
Poisson's ratio	0.35	0.33	0.35	0.21	0.23

of the resistances at welding force (III) reveals that the frictional motion overlay by a translational motion of the sheets can reduce the total resistance to about 50% of the value without motion overlay.

4 Simulative analysis of resistance spot welding process with and without oxide layer

The analysis of the resistance spot welding process using FEM was done with ANSYS® Academic Research Mechanical, Release 18.1. The investigations for the welding of aluminum alloys were carried out with the further developed model from [3]. The setup of the simulation model was accompanied by welding tests with and without motion overlay (see Fig. 11) at the test rig and subsequently validated.

For the multiphysical simulation, temperature-dependent mechanical, thermal, and electrical material data were determined (see Tables 2, 3, 4, and 5).

The plastic deformation is considered by using the flow curves of an EN-AW-6111 alloy in the T6 state and the CuCr1Zr alloy from the publication by Wan et al. [15]. As shown in Fig. 1, the enthalpy H has an influence on the temperature development. The calculation of the enthalpy is based on Eq. 2.

$$H(T) = \int_{T_0}^{T} \rho(T) \times C(T) dT \tag{2}$$

As can be seen in Tables 2 and 3, the temperature-dependent specific resistance ρ and the heat capacity C were determined only up to the melting temperature. The change in enthalpy during melting was determined from the data of Wang et al. [16].

Table 5 Mechanical material properties CuCr1Zr (electrode material)

Temperature (°C)	20	200	400	600	800	900
Young's modulus (GPa)	87.82	81.04	76.97	69.61	65.11	60.59
Shear modulus (GPa)	33.08	31.19	30.12	28.29	26.33	25.03
Poisson's ratio	0.33	0.3	0.27	0.31	0.33	0.34

The geometry modeling of the simulation model is analogous to the electrode caps and sheets used in the welding experiments. The use of the rotational symmetry of the resistance spot welding process enabled the reduction of a 3D geometry into a 2D model (see Fig. 13).

The discretization of the geometry into finite elements took place in the contact areas with a size of 0.2 mm. The element size of the remaining geometry is coarser with an average size of 0.375 mm. The multiphysics simulation is done in ANSYS by using the element "Plane223." The contact surfaces, which are identified in Fig. 13 with the numbers 1, 2, and 3, are constructed with the contact elements "Conta172" and "Targe169."

To calculate the heat generated at the contact surfaces the contact resistance is required. Different formulas can be used for the definition of contact resistance [7, 15]. In this work the equation from Wan et al. [15] is used.

$$\mathrm{ECR}\ (T,P) = 3\,d\left(\frac{\rho_1(T)+\rho_2(T)}{2}\right)\left(\frac{\sigma_{\mathrm{YS}}(T)}{P}\right)^{K} \tag{3}$$

In [14] the electrical contact resistance ECR (Eq. 3) is calculated similar to the simulation software SORPAS. The calculation is carried out by varying the pressure P and the temperature T by means of the specific material resistances of the contact partners ρ_1 and ρ_2 and the yield strength of the softer material σ_{YS}. Furthermore, the thickness of the contact layer d has an influence on the resistance. In this work, the typical value of 0.05 mm is assumed for d. With the exponent K, an adjustment of the contact resistance with respect to the oxide layer takes place. According to Wan et al. [15], the value can be varied between 1, which is used in this work, and 1.5.

The calculation of the heating within the contact zone takes place within the contact elements by the electrical contact

Table 4 Thermal and electrical material properties CuCr1Zr (electrode material)

Temperature (°C)	18	200	300	500	700	900
Specific resistivity (Ωm)	2.11E-08	3.25E-08	3.87E-08	5.43E-08	6.99E-08	9.81E-08
Thermal conductivity (W/m K)	326	305	291	281	310	268
Heat capacity (J/g K)	0.39	0.393	0.395	0.4	0.482	0.494
Density (g/cm^3)	8.882	8.803	8.755	8.656	8.549	8.425
Thermal expansion coefficient (ppm/K)	–	16.51	17.19	18.01	18.86	20.19

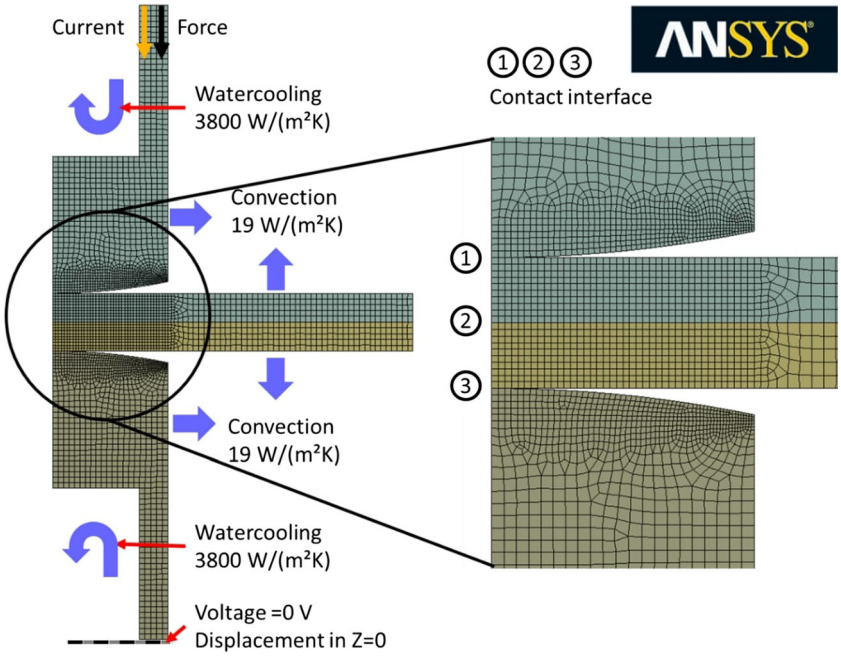

Fig. 13 Model structure of the FEM simulation, showing the boundary conditions, mesh, and contact interfaces

conductivity (ECC). For the heat transfer over the contact, the thermal contact conductivity TCC is used. The ECC (Eq. 4) is the inverse of the contact resistance ECR shown in Eq. 3.

$$\mathrm{ECC} = \frac{1}{\mathrm{ECR}} \tag{4}$$

The calculation of the TCC is done via the ECC, the Lorentz constant L, and the absolute temperature T according to Eq. 5.

$$\mathrm{TCC} = \mathrm{ECC} \cdot L \cdot T \tag{5}$$

As boundary conditions for the simulation of the resistance spot welding process (compare Fig. 13), the heat transfer coefficients for the heat convection and the water cooling were assumed to be 19 W/(m^2 K) and 3800 W/(m^2 K), respectively. The voltage and displacement in the Z-direction were each set to zero at the bottom of the lower electrode. The welding current and the electrode force are applied via the upper side of the upper electrode.

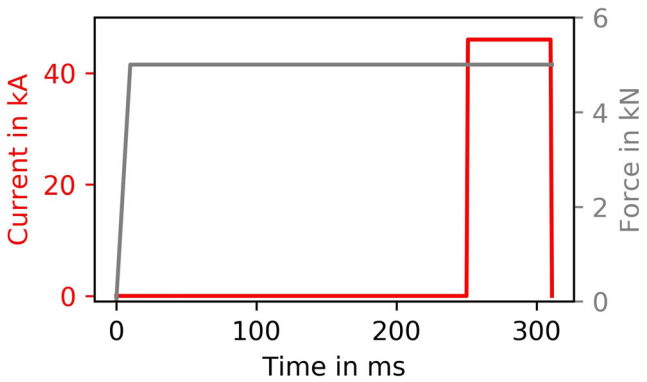

Fig. 14 Schematic force and welding current profile

The force profile and current profile for the simulation was determined according to the welding experiments and is shown in Fig. 14. The influence of force rise as well as force reduction is neglected in the simulation compared with the experiment (see Fig. 11a). For this reason, in the simulation, the force of 5 kN is applied within 10 ms and held over the entire simulation time. The welding current of 46 kA is applied with an upslope of 1 ms for a total of 60 ms. The downslope of the welding current is 1 ms.

The aim of the simulation is to analyze the difference in the formation of the weld nugget between welding processes with and without motion overlay. As could be shown from the preexaminations at the scratch tester and the experiments on the test rig, the resistance is approximately halved by the destruction of the oxide layer.

This means by doubling of the ECC and TCC, the effect of motion overlay can be achieved in the simulation. It was assumed that the oxide layer is broken during movement only between the electrodes and the sheets.

The initial results for the simulation without movement, with the ECR values calculated by Eq. 3, showed an undersized nugget. As already described, the ECR values are crucial for the development of heat in the contact zones and thus also for the formation of the weld nugget.

The equation for calculating the contact resistance according to SORPAS, on which the equation Eq. 3 is based, is described as comfortable but not well verified in the publication of Hamedi et al. [7]. For this reason, an

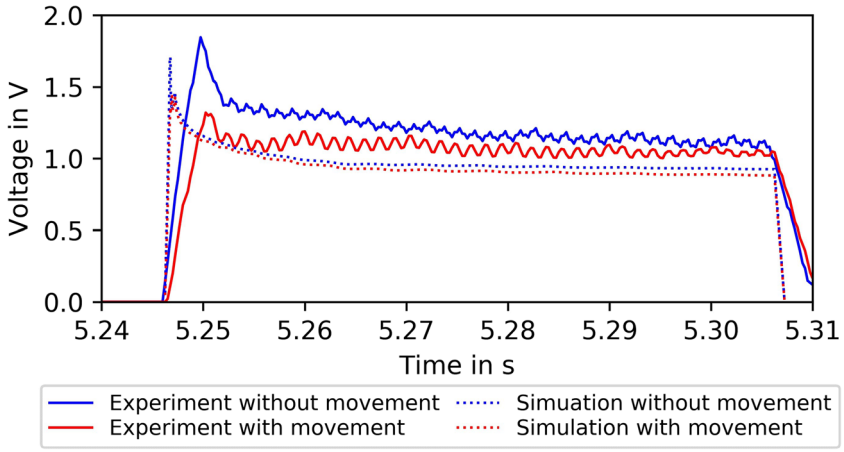

Fig. 15 Comparison of the voltage curves of experiment and simulation with and without movement

adjustment factor ζ (see Eq. 6) has been added in order to calibrate the values of Eq. 3.

$$\mathrm{ECR}_{\mathrm{cal}}\,(T,P,\zeta) = 3d\left(\frac{\rho_1(T)+\rho_2(T)}{2}\right)\left(\frac{\sigma_{YS}(T)}{P}\right)^{K} \times \zeta \tag{6}$$

The contact resistance has the biggest impact at the beginning of the welding process. As the process progresses, the influence of contact resistance decreases and the influence of the material resistance increases. For this reason, the factor ζ was determined by comparing the experimentally determined voltage peaks of the electrode voltage U_E at the beginning of the welding process, with those of the simulation. The waveform of the voltages of experiment and simulation with ζ matched is shown in Fig. 15. By adjusting the equation with $\zeta = 0.01$, an almost equal initial value of the voltage could be achieved. For better comparability, the times of the simulation in the diagram were adjusted to those of the experiment. The halving of the contact resistance, representing the breaking up of the oxide layer for the simulation of welding with motion overlay, led to a similar initial value of the voltage as in the experiments.

In Fig. 15, it becomes clear that the voltage values drop to an approximately constant level after the start of the process. The voltages in this area are mainly due to the material resistances. Compared with the simulation values, the experimental values are about 30% higher. In contrast to the simulation, all conductors and contact resistances in the measuring chain influence the experimental measurement. This results in a generally higher resistance. Another possibility is the material data used for the simulation. The aluminum alloy used is in T4 condition. This means that it has been solution annealed and cold aged. Since the experimental determination of the material data, further cold aging within the alloy can occur, which can lead to a higher material resistance. This influences the experiment but is not considered in the simulation.

The validation of the simulation model is done by comparing the nugget dimensions at the end of the welding process. Table 6 shows the average nugget diameters and heights of experiment and simulation.

The comparison of the nugget diameters shows approximately the same values. It can be seen that in the experiment as well as in the simulation, the nugget diameters decrease by about 2% due to movement. The nugget heights have approximately the same values of 2.7 mm for the experimentally determined values. In contrast, the simulated nugget heights of 3.9 mm resp. 3.6 mm are about 40% higher than the actual weld nuggets' heights. Furthermore, the height is reduced by 7.5% by the motion overlay in the simulation. The lower nugget height of the experiments in comparison with the simulation may be due to the shunt-effect induced by the clamping of the sheets. Also, the approximation of the real current profile with the idealized profile in Fig. 14 may lead to differences.

The difference in the temperature field at the end of the weld current flow for both simulation models is shown in Fig. 16.

Table 6 Comparison of the nugget dimensions of experiment and simulation

Movement	Nugget diameter experiment (mm)	Nugget diameter simulation (mm)	Nugget height experiment (mm)	Nugget height simulation (mm)
Without	7.88	8.0	2.73	3.9
With	7.78	7.8	2.70	3.6

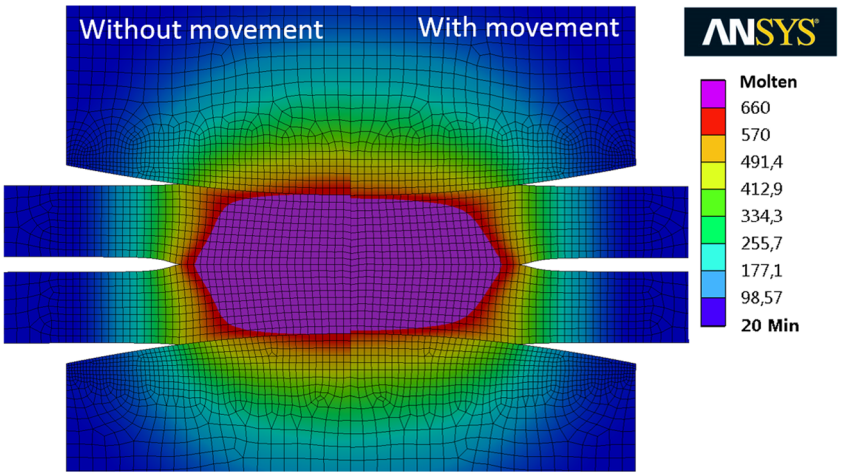

Fig. 16 Representation of the temperature distribution at the end of the weld current flow without movement (left) and with movement (right)

The simulation without movement (Fig. 16, left) has a propagation of the weld nugget up to the sheet surface. In the simulation with movement (Fig. 16, right), the molten area ends about 0.1 mm under the electrode. In addition, the heat input into the electrode is lower. This can be justified by the law of Joule (Eq. 1). By breaking up the oxide layer in the contact area between the electrode and the sheet, the contact resistance decreases and less heat is generated. For a better understanding of the temperature development between the electrode and the sheet, the temperature-time profile for a node on the axis of symmetry in the region of the contact electrode sheet is shown in Fig. 17.

The temperature development between the electrode and the sheet shows that the motion overlay can reduce the temperature by about 50 K. This means that the alloying of aluminum to copper is reduced, which would result in an increase of the electrode life. But as the comparison in Table 6 has shown, the lens heights from the simulation do not match those from the experiments. Thus, this theory cannot be finally proven.

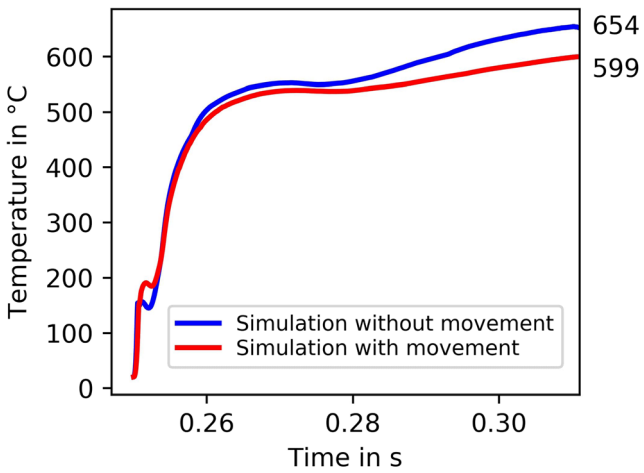

Fig. 17 Representation of the temperature development at the contact interface electrode sheet without movement (blue) and with movement (red)

Figure 18 shows a cross-section of a sample welded without motion overlay (a) and with motion overlay (b). The heat-affected zone (bright seam) shows a horizontal extension of approx. 0.1 mm and a vertical extension of approx. 0.3 mm in all tests. Despite the same lens heights, it can be seen that the heat-affected zone in the sample a reaches as far as the sheet surface, which is not the case within sample b. This can be explained by the sheet thickness, which is 0.2 mm higher in b after welding. The higher thickness is assumed to be caused by less total heating of the sheets in b because of the lower contact resistance inducing less heat at the sheet surface. These experimental findings suggest that the lower heating in the contact of electrode and sheet reduces the thermal stress on the electrode. Thus, an increase in the electrode life is likely.

In comparison, virtually, no differences in the deformation of the sheet metal could be determined in the simulation shown in Fig. 16. The deformation is approximately the same for both simulation models. This difference between experiment and simulation could be attributed to the flow stress curves used for modeling. The values correspond to the EN-AW-6111 aluminum alloy in T6 condition. The aluminum alloy used in the experiments is in the T4 state and thus has a lower strength. It can be expected that the simulation results will be approximated to the experiment by adjusting the flow stress curve. In addition, the overshoot of the electrode force due to electromagnetic force was not taken into account in the simulation. This could also be the reason for the deviating plastic deformation comparing experiment and simulation.

At this time, no precise statements can be made regarding the influence of the motion overlay on the increase of

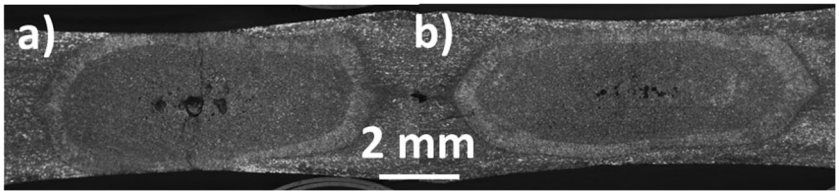

Fig. 18 Cross-section polishes of the weld nuggets without movement (**a**) and with movement (**b**)

electrode life. A larger test scope must be realized in order to make a reliable statistically verified statement and to determine the individual parameter dependencies in this complex process. In addition, the FE simulation model must be further developed with regard to the material data and a more precise representation of the real experiments (current and force curves).

5 Summary and outlook

In this article, the resistance spot welding process with additional motion overlay was briefly introduced and its complex interdependencies were illustrated. By means of an analogy experiment, the mechanism of the destruction of the oxide layer could be clarified and reproduced in a simulative analysis. The experiments showed that even at low contact forces of the electrode a destruction of the oxide layer can be achieved. However, the accumulation of material in front of the electrode should be considered.

The test rig developed for the experimental investigation of resistance spot welding processes with motion overlay was presented with regard to the measurement chain set up for data acquisition in the experiments. As an example for the execution and evaluation of the experiments, a welding test with frictional motion overlay before the weld current flow was explained as an example. On the basis of the experiments carried out with motion overlay, the effect of breaking up the oxide layer could be demonstrated. The reduction of the total resistances to approx. 50% of the initial value without motion overlay, which could already be observed in the analogy experiments, could be proven.

In the following simulative analysis of the resistance spot welding process with motion overlay, the destruction of the oxide layer was considered by parameterization of the correspondingly reduced contact resistance. In addition, the contact resistance parameter ECR determined by the equation of Wan et al. had to be adjusted with a factor ζ determined empirically from the welding tests. On the basis of the results of the simulation, the effect of the destruction of the oxide layer could be qualitatively reconstructed. In the process with motion overlay and correspondingly lower contact resistance between electrode and sheet metal, the heat generation in this area is also lower, and consequently, the thermal load on the electrode is reduced. The comparison with the experiment (cross-section polish) showed that the size of the weld nugget in the simulation was estimated to be too large (especially the height of the nugget). A realistic representation of the deformation in the zone of the weld nugget is therefore not available, which is probably due to the different yield stress curves and the parameterization of the normal force curve in the simulation. An enhancement of the simulation model has to be implemented in order to be able to represent the welding tests in the best possible way.

In the future, more extensive test series will be carried out for the experimental determination of parameter dependencies in the destruction of the oxide layer. The rolling and combined motion overlay (cf. a and b in Fig. 2) and the motion overlay synchronous to the weld current flow will also be investigated.

The simulation models developed will be further improved. This concerns in particular the determination and parameterization of the material parameters (flow stress curve) as well as the improved mapping of current and force curves in the FE simulation. In addition, it must be checked whether the clamping of the test sheets can lead to a shunt connection, which has to be taken into account in the simulation.

Funding information This research was funded by the German Research Foundation (DFG) within the project “Development of a methodology for simulation-based analysis of resistance spot welding processes with motion overlay on the example of aluminium materials” under the grant numbers GR1458/62-1 resp. FU307/11-1.

References

1. Kunze S (2014) Beitrag zur Erhöhung der Prozesssicherheit beim Punktschweißen und Punktschweißkleben von Aluminiumkarosseriewerkstoffen. Dissertation. Shaker Verlag, Aachen, Germany
2. Heilmann S, Zwahr C, Knape A et al (2018) Improvement of the electrical conductivity between electrode and sheet in spot welding process by direct laser interference patterning. Adv Eng Mater 114: 1700755. https://doi.org/10.1002/adem.201700755
3. Heilmann S, Mathiszik C, Merx M, Müller J, Zschetzsche J, Ihlenfeldt S, Füssel U (2016) Numerical simulation strategies and test setup for resistance spot welding process with motion overlay. Weld World 61:35–46. https://doi.org/10.1007/s40194-016-0403-z
4. Rippl P (2006) Verfahren und Vorrichtung zum elektrischen Punktschweißen(DE 102005001341 B3) https://www.freepatentsonline.com/DE102005001341B3.html. Accessed 14 May 2019
5. Sigler DR, Schroth JG, Karagoulis MJ (2013) Electrode for spot welding. (US20130306604 A1) https://www.google.com/patents/US20130306604. Accessed 14 May 2019

6. Sigler DR, Carlson BE, Janiak P (2013) A recently developed electrode design features multiple protruding rings that penetrate oxide layers by straining the aluminum sheet surface during welding. Weld J 92(6):64–72
7. Hamedi M, Atashparva M (2017) A review of electrical contact resistance modeling in resistance spot welding. Weld World 61: 269–290. https://doi.org/10.1007/s40194-016-0419-4
8. Wang SC, Wei PS (2001) Modeling dynamic electrical resistance during resistance spot welding. J Heat Transf 123(3):576. https://doi.org/10.1115/1.1370502
9. Song Q, Zhang W, Bay N (2005) An experimental study determines the electrical contact resistance in resistance welding. Weld J 84(5): 73S–76S
10. Crinon E, Evans JT (1998) The effect of surface roughness, oxide film thickness and interfacial sliding on the electrical contact resistance of aluminium. Mater Sci Eng A 242(1–2):121–128. https://doi.org/10.1016/S0921-5093(97)00508-X
11. James PS, Chandler HW, Evans JT, Wen J, Browne DJ, Newton CJ (1997) The effect of mechanical loading on the contact resistance of coated aluminium. Mater Sci Eng A 230(1–2):194–201. https://doi.org/10.1016/S0921-5093(97)00020-8
12. Deng L, Li Y-B, Carlson BE, Sigler DR (2018) Effects of electrode surface topography on aluminum resistance spot welding. Weld J 97(4):120–132. https://doi.org/10.29391/2018.97.011
13. Deutsche Norm DIN EN ISO 5821 (2009) Resistance welding - Spot welding electrode caps
14. Ihlenfeldt S, Müller J, Merx M (2017) Widerstandspunktschweißen mit Bewegungsüberlagerung – Entwicklung einer Versuchseinrichtung als mechatronisches System. In: Bertram T, Corves B, Janschek K (eds) Fachtagung Mechatronik 2017: Dresden (09.03.-10.03.2017). Technische Universität, Dresden
15. Wan Z, Wang H-P, Wang M, Carlson BE, Sigler DR (2016) Numerical simulation of resistance spot welding of Al to zinc-coated steel with improved representation of contact interactions. Int J Heat Mass Transf 101:749–763. https://doi.org/10.1016/j.ijheatmasstransfer.2016.05.023
16. Wang B, Hua L, Wang X, Song Y, Liu Y (2015) Effects of electrode tip morphology on resistance spot welding quality of DP590 dual-phase steel. Int J Adv Manuf Technol 83:1917–1926. https://doi.org/10.1007/s00170-015-7703-0